# Optical Anisotropy in Vertically Oriented $TiO_2$ Nanotube Arrays

Yun Zhang,[1 *] Samira Farsinezhad,[1] Benjamin Wiltshire,[1] Ryan Kisslinger,[1] Piyush Kar,[1 *] and Karthik Shankar[1, 2 *]

[1]*Department of Electrical and Computer Engineering, University of Alberta, 9211-116 St, Edmonton, Alberta, T6G 1H9, Canada*
[2]*NRC National Institute for Nanotechnology, 11421 Saskatchewan Dr NW, Edmonton, AB T6G 2M9, Canada*

*E-mail addresses of corresponding authors: yun10@ualberta.ca, pkar1@ualberta.ca, kshankar@ualberta.ca

**Abstract**

Nanofabricated optically anisotropic uniaxial thin films with deep submicron feature sizes are emerging as potential platforms for low-loss all-dielectric metamaterials, and for Dyakonov surface wave-based subwavelength optical confinement and guiding at interfaces with isotropic media. In this context, we investigate the optical properties of one such uniaxial platform, namely self-organized titania nanotube arrays (TNTAs) grown by the bottom-up nanofabrication process of electrochemical anodization on silicon wafer substrates, and subsequently annealed at different temperatures, i.e. 500 °C and 750 °C. We performed detailed quantitative analysis of the structure of the TNTAs using X-ray diffraction and Raman spectroscopy, which revealed a measurable phonon confinement in TNTAs annealed at 500 °C. Variable angle spectroscopic ellipsometry was used to investigate the optical anisotropy in two kinds of TNTAs - those constituted by anatase-phase and those containing a mixture of anatase and rutile phases. Both kinds of TNTAs were found to have positive birefringence ($\Delta n$) exceeding 0.06 in the spectral region of interest while mixed phase TNTAs exhibited $\Delta n$ as high as 0.15. The experimentally measured anisotropy in the refractive index of the TNTAs was compared with the predictions of two different effective medium approximations incorporating the uniaxial geometry. The measured value of $\Delta n$ for TNTAs exceeded that of bulk anatase single crystals, indicating the potential of nanostructured dielectrics to outperform dielectric crystals of the same material with respect to the magnitude of the achievable directional refractive index contrast.

**Key Words:** nanophotonics; nanostructured dielectrics; phonon confinement; sculptured thin films; specular reflectance; nanorod arrays; nanohole arrays; photonic crystal;

## 1. Introduction

Anodically formed nanoporous alumina thin films and membranes (AAO) have been used as a platform to fabricate and investigate metamaterials, particularly because of the controllable formation of deep sub-wavelength features by a non-lithographic bottom-up self-organization process [1]. $TiO_2$ nanotube arrays (TNTAs) formed by electrochemical anodization (see Figure 1) constitute a highly ordered and vertically oriented nanostructure similar to AAO but with some important advantages [2]. The much higher refractive index of $TiO_2$ enables greater refractive index contrast between the $TiO_2$ matrix and the air inclusions. The wall-thickness and inter-tubular spacing of TNTAs can be tuned within a limited range while the nanotube diameter can be controlled over a much wider range from 10 nm–1000 nm [3-5]. A related architecture called $TiO_2$ nanorod arrays (TNRAs) consists of vertically oriented pillars of anatase or rutile [6, 7]. While aluminum oxide is an insulator, both the anatase and rutile forms of titanium dioxide are wide bandgap *n*-type semiconductors, due to which TNTAs (and TNRAs) are used as the active layer in photocatalysts [8-10], photoelectrodes [11, 12] and biosensors [13, 14], and as an electron transport layer in halide perovskite-, quantum dot- and dye-sensitized solar cells [15-21], organic bulk heterojunction solar cells [22, 23], batteries and super-capacitors [24-26], and memristors [27, 28]. Furthermore, self-organized $TiO_2$ nanotubes have been used to form 1D, 2D and 3D photonic crystals without recourse to lithographic patterning [29-36]. Therefore $TiO_2$ nanotube arrays offer a potentially superior platform for both fundamental studies and practical applications of metamaterials.

When a weakly anisotropic uniaxial metamaterial such as AAO is filled with noble metal nanowires, the resulting composite is strongly optically anisotropic with $\mathrm{Re}(\varepsilon_{\parallel}) \leq 0$ and $\mathrm{Re}(\varepsilon_{\perp}) > 0$ over a certain spectral range, relative to the axis of the cylindrical nanochannels of AAO [37-39]. Such metallodielectric metamaterials have been used to demonstrate superlens imaging, broadband negative refraction, high *Q*-factor refractive index sensing of analytes and nonlinear optical enhancement [40-43]. However metallodielectric metamaterials are lossy and consequently exhibit limited performance in a wide range of applications due to energy dissipation. In response, there has been a concerted move toward all-dielectric metamaterials which exploit optical anisotropy and/or Mie resonances to generate unusual electromagnetic effects in practical device applications [44-52]. In contrast to lossy surface plasmon polaritons, Dyakonov-like surface wave packets at the interface between optically anisotropic dielectric

nanostructures and an isotropic medium, have shown promise for loss-free subwavelength directional guiding of light [53-57]. $TiO_2$ nanotube arrays are particularly intriguing platforms for all-dielectric metamaterials because they have two distinct sources of anisotropy - (i) morphological and (ii) structural/crystallographic. The source of morphological anisotropy is the uniaxial geometry evident in Figure 1, and is the same as seen in any array of vertically oriented nanopores or nanorods ("so-called wire metamaterial"). The structural anisotropy originates in the tendency of the nano-crystallites constituting the nanotube walls to be either randomly aligned or aligned along the *c*-axis of tetragonal anatase and rutile lattice structures, depending on the growth conditions [58, 59]. Since both anatase and rutile are birefringent crystals, aligned crystallites in the nanotube walls can further amplify the refractive index contrast as compared to randomly oriented crystallites. While rutile has a large birefringence ($\Delta n = n_e - n_o \sim 0.27$), anatase has a smaller value of $\Delta n$ (~ 0.07) [60, 61]. The optical anisotropy in TNTAs has never been previously measured, and all prior reports have assumed an isotropic permittivity even though TNTAs are clearly uniaxial as seen in Figure 1. In this report, we measured and modeled the anisotropic permittivity of TNTAs on Si wafer substrates.

## 2. Experimental

250 nm-thick titanium (purity >99.999%) films were deposited onto piranha-cleaned *n*-type <111> oriented silicon wafers using a planar DC magnetron sputtering system. The deposition conditions used were designed to maximize film smoothness by recourse to atomic peening [62]. TNTAs were fabricated by anodization of Ti thin films in ethylene glycol (EG)-based organic electrolyte containing 0.09 M (0.3 wt %) $NH_4F$ and 9 vol% deionized water at a voltage of 40 V vs. a graphite counter-electrode placed at a distance of 2 cm from the anode. Following anodization, the residual electrolyte and debris were removed by rinsing the samples with methanol. As-prepared TNTA samples were then annealed in a tube furnace at 500 °C for 2.5 hours in flowing oxygen to generate TNTAs consisting of the anatase phase. The heating and cooling rates were 5 °C $min^{-1}$. Other as-anodized titania nanotube samples were annealed at 750 °C for 2.5 hours in flowing oxygen to obtain rutile phase TNTAs.

Morphological characterization of the pore diameter, wall-thickness and length of the nanotubes was undertaken using a Zeiss Sigma field emission scanning electron microscope (FESEM). Reflection spectra were measured using a variable angle spectroscopic ellipsometer

(VASE Woollam Inc, USA) with unpolarized reflectance scan. X-ray diffraction patterns (XRD) of the TNTAs on silicon were obtained using a Bruker D8 Discover instrument with a sealed Cu tube X-ray source. Raman spectra were obtained using a Nicolet Almega-XR Raman microscope excited by a 532 nm laser source. Spectroscopic ellipsometry measurements were carried out using the variable angle spectroscopic ellipsometer (VASE Woollam Inc, USA) in the 600 nm-1200 nm wavelength range with a spectral resolution of 1 nm, and at incident angles from 25° to 75° in steps of 25°. Three separate sets of data were obtained at each wavelength. A multilayer model was used for data fitting in order to extract the thickness and refractive index of each layer.

## 3. Results and Discussion

*3.1 Morphology and uniformity of the $TiO_2$ nanotube arrays*

The morphologies of the TNTAs are shown in FESEM images (Figure 2), which illustrate a porous surface with a cylindrical profile (Figures 2(c) and 2(d)). The nanotubes have an average inner diameter of ~ 80 nm when annealed at 500 °C (Figure 2(a)), which decreases to ~ 50 nm when annealing temperature is raised to 750 °C (Figure 2(c)). We attribute the decrease in inner diameters of the nanotubes with increasing annealing temperature to the high-temperature induced outward diffusion of $TiO_2$ at 750 °C that narrows down the pores. Moreover, we observed an increase in the overall external diameter of the $TiO_2$ nanotubes than what is observed in nanotubes formed by anodization of Ti foil. The overall tube diameter increase may explained by the fact that our nanotubes were formed out of sputtered Ti films on Si substrates and also due to our use of high water content EG-based anodization electrolytes. It is well established that sputtered Ti films on non-native substrates, such as Si and fluorine doped tin oxide (FTO) glass, can differ from Ti foils in their crystallographic texture and grain sizes [63]. Differences in crystallographic texture and grain sizes lead to variations in the pitting and anodic oxidation processes of Ti [64, 65]. e surmise that Ti sputtered on Si can support larger pit sizes formed by field-assisted dissolution of Ti in the electrolyte used, resulting in larger nanotube diameters. The length of TNTAs is ~ 600 nm (as shown in Figures 2(b) and 2(d)), obtained by anodization of the vacuum deposited 250 nm Ti thin film on the Si wafer. The thickness of the $TiO_2$ carpet (i.e. the length of the TNTAs) is dictated by the thickness of the sputtered Ti layer

which was varied in the range 50 – 500 nm for different samples. The uniformity of the sputtered Ti film is affected by its thickness, in that the thicker the sputtered film the less uniformity it will have. The refractive indices estimated purely using effective medium approximations (EMAs) in this work are independent of film thickness. However, considering that the $TiO_2$ carpet produced by longer nanotubes will be rougher, thus producing more deviations between the ellipsometric data and the results of effective medium calculations, the optimal thickness was chosen to achieve a balance between the uniformity of the sputtered Ti layer and the accuracy of the ellipsometric output. On the basis of our experiments, we found that 250 nm is the optimal thickness of the Ti layer.

For ellipsometric analysis of the optical properties of the TNTAs, a necessary attribute is a highly smooth surface enabling reflectivity measurements. For this reason, atomically smooth monocrystalline silicon wafers were used as the growth substrate since we have previously shown that substrate smoothness has a determinative effect on the uniformity of the resulting nanotubes [63]. Furthermore, sonication and reactive ion etching treatments used to remove anodization debris subsequent to nanotube growth, were deliberately avoided since these treatments also produce a higher dispersion in the heights of the individual nanotubes, which in turn, produces scattering and reduces the reflectivity. The use of fluoride-bearing ethylene glycol-based electrolytes to perform the anodic growth of TNTAs without subsequent cleaning typically results in a higher $TiO_2$ fill-fraction than aqueous electrolytes where etching is stronger and no redeposition of $TiO_2$ occurs.

The high optical quality of the TNTAs used in this study is evident from the observation of interferometric fringes in the reflection spectra shown in Figure 1. The thickness of the titania nanotube-air composite thin film can be approximately calculated from the spacing of the interference fringes through use of the following expression [66]:

$$t = \frac{\lambda_1 \lambda_2}{2(\lambda_2 - \lambda_1)\sqrt{n^2 - \sin^2\theta}} \qquad (1)$$

In Eqn. (1), $t$ is the film thickness, $n$ is the average ordinary refractive index in this case, $\theta$ is the angle of incidence with respect to the sample, and $\lambda_1$ and $\lambda_2$ are the wavelengths of adjacent crests (or troughs) in the interference pattern. The calculated film thicknesses are 637.81 nm and 774.18 nm for TNTAs annealed at 500 °C and 750 °C respectively. The calculated results are in

reasonable agreement with what is observed from the FESEM images, as shown in Figures 2(b) and 2(d).

*3.2 Structure of the $TiO_2$ nanotube arrays*

Figure 4 shows XRD patterns of TNTAs after furnace annealing at 500 °C and 750 °C. The initially amorphous as-anodized TNTAs are crystallized by annealing. By comparing the pattern in Figure 4(a) with the standard pattern of anatase $TiO_2$, we found that all the diffraction peaks of the 500 °C annealed TNTAs (black curve) correspond to the lattice planes of anatase $TiO_2$. No rutile phase is observed for the 500 °C annealed TNTAs. Figure 4(a) also shows the XRD patterns of TNTAs after furnace annealing at 750 °C for 2.5 hours (red curve) which are transformed into a mixture of anatase and rutile phases as evidenced by reflections corresponding to both phases. These results are in line with prior reports on the structural transformation in TNTAs upon annealing at elevated temperatures [67, 68]. Crystallite sizes ($s$) for anatase and rutile grains were determined from the anatase (101) and rutile (110) peaks (Figure 4 (a)) by using Scherrer equation, which is as follows:

$$s = \frac{K\lambda}{\beta \cos\theta} \qquad (2)$$

In Eqn. (2), $K$ is assumed to be one, $\lambda$ is 0.154 nm (i.e. the incident x-ray wavelength), $\beta$ is the full-width at half maximum (FWHM) of the peaks, and $\theta$ is Bragg angle. The size of anatase grains in the TNTAs annealed at 500 °C is 17.39 nm and the same in TNTAs annealed at 750 °C is 35.82 nm. The size of rutile grains in TNTAs annealed at 750 °C is 29.88 nm. The intensities of rutile (110) and anatase (101) peaks in XRD pattern of TNTAs annealed at 750 °C was used to estimate the percentage of rutile ($p$) [69], according to the following relationship:

$$p = \frac{Ir}{0.884.Ia + Ir} \qquad (3)$$

In Eqn. (3), $Ia$ is the intensity of anatase (101) peak and $Ir$ is the intensity of rutile (110) peak. Using Eqn. (3), $p$ is 29 % in our TNTAs annealed at 750 °C.

Raman spectra for the TNTAs annealed at 500 °C and 750 °C are shown in Figure 3 (b). The presence of anatase phase alone in the 500 °C annealed TNTAs (black curve in Figure 4(a) and Figure 4(b)) is also confirmed by Raman peaks near 143, 395, 519 and 633 $cm^{-1}$

corresponding to the $E_g$, $E_g$, $B1_g$, $A1_g$ and $E_g$ modes respectively [70]. The aforementioned peaks also appear in the Raman spectrum of 750 °C annealed TNTAs (red curve in Figure 4(b)) at 141, 394, 519 and 635 $cm^{-1}$ corresponding to the $E_g$, $B_{1g}$, $B1_g$ and $E_g$ modes respectively. There is an additional $E_g$ peak at 198 $cm^{-1}$ due to the greater degree of anatase crystallization at 750 °C. As indexed, the peak positions and Raman modes predominantly correspond to anatase, although a low intensity rutile $E_g$ peak at 440 $cm^{-1}$ is observed [71, 72]. The intense peak at 141 $cm^{-1}$ likely has contributions from both anatase $E_g$ and rutile $B_{1g}$ modes.

Unlike larger grains in bulk $TiO_2$, $TiO_2$ nanotubes have crystalline grains in the lateral direction (i.e. in the substrate plane) that are usually small with a size less than 20 times the lattice parameter. At these sizes, the phonon wave function decays to small values near grain boundaries, leading to diminished phonon lifetimes. Furthermore, the phonon contribution is from the entire Brillouin zone compared to crystals with larger grain sizes, where phonon dispersion is from the center of the Brillion zone. Therefore, we have, herein, analyzed the phonon confinement effect in the TNTAs. Generally, the phonon confinement effect in $TiO_2$ nanocrystals is analyzed from asymmetric broadening and shifting of the $E_g$ peak of anatase, which is usually the most intense Raman peak and the one that is most affected by crystalline grain size. The other Raman modes in anatase (the $A_{1g}$ peak, the two $B_{1g}$ and the two $E_g$ peaks) also undergo broadening and blue-shifting as a result of particle size, but to a lesser extent. [73] To analyze the phonon confinement effect, we performed Lorentzian fitting of the main peaks.

FWHMs of the Raman peaks were obtained from their Lorentzian model fits (as shown in Figures 4 (b), 5(c), and 5(d)). Table 1 shows the FWHM, phonon lifetime and crystallite sizes of the TNTAs annealed at 500 °C and 750 °C. The narrower and sharper Raman peaks are due to improved crystallinity caused by annealing that is indicated by their narrower FWHMs and longer phonon lifetimes. The low frequency $E_g$ peaks are close to those reported for the Eg (144 $cm^{-1}$) mode for $TiO_2$ nanotubes. [73, 74] The FWHMs and phonon lifetimes for the $B_{1g}$ and high frequency $E_g$ modes match well with a similar Gaussian confinement model for the Eg (144 $cm^{-1}$), B1g (397 $cm^{-1}$) and Eg (639 $cm^{-1}$) peaks and were measured to be 7.5 $cm^{-1}$, 20 $cm^{-1}$ and 20 $cm^{-1}$ respectively. [73] The relatively blue-shifted $E_g$ peak of the 500 °C annealed TNTAs is likely because of their smaller (101) anatase crystallite size compared to the same in 750 °C annealed TNTAs. The anatase $B_{1g}$ peak at 395 $cm^{-1}$ for the 500 °C annealed TNTAs lies closer to the bulk $TiO_2$ value (397 $cm^{-1}$, [74]) than the same, at 394 $cm^{-1}$, for the 750 °C annealed

TNTAs, implying consistency with the shifts of the low frequency $E_g$ peaks. Raman peaks for the high frequency $B_{1g}$ and $E_g$ modes for anatase in the TNTAs are red-shifted from their bulk values of 519 $cm^{-1}$ and 639 $cm^{-1}$, respectively.

We applied a time-energy uncertainty relation (Eqn. (4)) to obtain phonon lifetimes for the Raman peaks of the TNTAs. [75]

$$\frac{\Delta E}{\hbar} = \frac{1}{\tau} \qquad (4)$$

In Eqn. (4), $\Delta E$ is the FWHM, $\hbar = 5.3\text{x}10^{-12}$ $cm^{-1}s$, and $\tau$ is the phonon lifetime. $\tau$ for the 395 $cm^{-1}$ $B_{1g}$ Raman mode, thus obtained, was 0.12 ps for the TNTAs annealed at 500 °C, and 0.19 ps for the TNTAs annealed at 750 °C. The shorter phonon lifetime for TNTAs annealed at 500 °C is in agreement with the phenomenon of phonon wave function decay to low values near grain boundaries of the small crystallites comprising the TNTAs.

**Table 1.** FWHM and phonon lifetime data derived from model for anatase and mixed anatase and rutile

| TNTAs annealed at 500 °C | | | TNTAs annealed at 750 °C | | |
|---|---|---|---|---|---|
| Raman mode | $\Delta E$ ($cm^{-1}$) | $\tau$ (ps) | Raman peaks | $\Delta E$ ($cm^{-1}$) | $\tau$ (ps) |
| Anatase $E_g$, 143 $cm^{-1}$ | 17.45 | 0.30 | Anatase $B_{1g}$ + Rutile $B_{1g}$, 141 $cm^{-1}$ | 13.14 | 0.40 |
| Anatase $B_{1g}$, 395 $cm^{-1}$ | 31.38 | 0.17 | Anatase $B_{1g}$, 394 $cm^{-1}$ | 19.46 | 0.27 |
| Anatase $E_g$, 633 $cm^{-1}$ | 34.67 | 0.15 | Anatase $E_g$, 635 $cm^{-1}$ | 30.78 | 0.17 |

*3.3 Anisotropic optical properties of uniaxial $TiO_2$ nanotube arrays*

For a two-component medium such as shown in Figure 1, Bruggeman (BR) and Maxwell-Garnett (MG) are the most frequently used effective medium approximations (EMAs) to obtain the effective optical properties of nanocomposites. While BR theory is valid for all filling fractions of the two components, MG theory is only valid for dilute systems wherein the volumetric filling fraction of the guest material in the host matrix is low. Since the titania component has a high filling fraction in the nanotube arrays as shown in Figure 2, we decided to

use the BR approximation for uniaxial media according to which the ordinary ($\varepsilon_o$) and extraordinary ($\varepsilon_e$) components of the effective permittivity are given by [76]

$$\frac{(1-f)\left(\varepsilon_{air}-\varepsilon_o\right)}{(\varepsilon_{air}+\varepsilon_o)/2}+\frac{f\left(\varepsilon_{TiO_2}-\varepsilon_o\right)}{(\varepsilon_{TiO_2}+\varepsilon_o)/2}=0 \tag{5}$$

$$\frac{(1-f)\left(\varepsilon_{air}-\varepsilon_e\right)}{\varepsilon_e}+\frac{f\left(\varepsilon_{TiO_2}-\varepsilon_e\right)}{\varepsilon_e}=0 \tag{6}$$

Eqns. (1) and (2) highlight the importance of first estimating the volumetric fill fraction $f$ of $TiO_2$ in the air matrix in the TNTAs. $f$ depends on the diameter, wall-thickness and packing of the nanotubes, and can vary substantially for different growth conditions e.g. varied anodization and etching conditions. For the TNTAs in Figure 1, $f$ is given by [77, 78]

$$f=\frac{\dfrac{2(a-b)}{a}-\left(\dfrac{(a-b)}{a}\right)^2}{\dfrac{2\sqrt{3}}{\pi}\left[1+\left(\dfrac{\beta-2a}{2a}\right)^2\right]} \tag{7}$$

In eq. (7), $a$ is the outer radius of the nanotubes, $b$ is the inner radius and $\beta$ is the center-to-center spacing as shown in Figure 6. Applying Eqn. (3) to the dimensions of the TNTAs in this study (see Figure 2), we found $f$ = 0.62 for the anatase-phase TNTAs and $f$ = 0.68 for anatase-rutile mixed phase TNTAs.

The BR expressions in Eqns (1) and (2) for the effective optical permittivity do not take into account the cylindrical symmetry of the two-component uniaxial medium constituted by the TNTAs. For an array of vertically oriented, parallel cylinders and cylindrical shells (assumed infinite in length), the effective permittivities of the nanocomposite $\varepsilon_{eff}^{\parallel}$ parallel to, and $\varepsilon_{eff}^{\perp}$ perpendicular to the axes of the cylinders are given by [79]

$$\varepsilon_{eff}^{\parallel}=\varepsilon_{air}+f\left(\varepsilon_{TiO_2}-\varepsilon_{air}\right) \tag{8}$$

$$\varepsilon_{eff}^{\perp} \approx \varepsilon_{air}\left(1+2f\frac{\Delta_{eff}}{\left[1-f\Delta_{eff}\right]}\right) \tag{9}$$

In (8) and (9),

$$\Delta_{eff} = \frac{\varepsilon_{air}-\varepsilon_{TiO_2}}{\varepsilon_{air}+\varepsilon_{TiO_2}}\left(a^2-b^2\right)\Big/a^2-\left(\frac{\varepsilon_{air}-\varepsilon_{TiO_2}}{\varepsilon_{air}+\varepsilon_{TiO_2}}\right)^2 b^2 \tag{10}$$

With $\varepsilon_{eff}^{\parallel}$ the same as $\varepsilon_e$, and $\varepsilon_{eff}^{\perp}$ the same as $\varepsilon_o$. The extinction coefficient $k$ (imaginary part of the complex refractive index) of the TNTAs is assumed to be negligibly small, which is a valid assumption for wavelengths larger than 600 nm, since the sub-bandgap absorption of TNTAs due to defects and impurities typically extends only to ~ 600 nm [80]. Since the optical extinction of $TiO_2$ inclusive of the Urbach tail can be ignored in the wavelength region of interest (600 nm – 1200 nm), the effective refractive index $n_{\text{eff}}$ is given by the square-root of the effective optical permittivity. The effective ordinary and extraordinary refractive indices of TNTAs calculated using the published values for the permittivity of polycrystalline $TiO_2$ [81], and the equations for a Bruggeman medium (BR) and a medium containing vertically oriented, parallel cylindrical inclusions (CYL), are shown in Figure 7.

The rutile phase of $TiO_2$ has a much higher refractive index than anatase, a fact reflected in Figure 7 in the values of both the refractive index for extraordinary rays $n_e$ and the refractive index for ordinary rays $n_o$, being higher for rutile-phase TNTAs compared to anatase-phase TNTAs. Figure 7 indicates $n_e$ to be significantly higher than $n_o$ for all the cases considered, and such a high directional refractive index contrast due to anisotropy is desirable for all-dielectric metamaterials as previously discussed. However the calculated birefringence ($\Delta n = n_e - n_o$) is smaller when using the BR effective medium approximation.

Variable angle spectroscopic ellipsometry (VASE) [82] is a powerful non-destructive technique for optical and electronic characterization of materials. It measures the change in polarization state of transmitted or reflected light from a sample surface. Variable angle measurements help to filter multiple solutions of the ellipsometric equation set, and help choose the true solution [83] while the spectroscopic measurements enhance the information content by providing the dispersion of optical parameters [84]. The interaction of polarized light with a

medium is described by the complex Fresnel reflection coefficients $r_s$ and $r_p$ (for *s*- and *p*-polarized light respectively) which link the amplitude and phase of the reflected light to the incident light. The measured quantity (a ratio of the Fresnel coefficients) is usually expressed as a function of Ψ and Δ [82]

$$\frac{r_p}{r_s} = \tan\Psi\, e^{i\Delta} \qquad (11)$$

The refractive index (*n*) and extinction coefficient (*k*) which are analytically related to these two parameters (Ψ and Δ) can thus be measured using ellipsometry at an oblique incidence. By applying a numerical analysis based on a mathematical model of the optical dispersion of the medium, parameters such as the thickness and optical constants of a certain layer of the multilayer sample can be determined.

The collected data is shown in Figure 8, which are dispersion patterns of the measured quantities Ψ and Δ. The determination of the optical parameters is based on choosing the appropriate model that enables the best fitting of these dispersion curves. A three-layer model was first built for data fitting. The bottom layer in this model was the monocrystalline silicon substrate. The second layer consisted of the oxide barrier layer which is transparent in the measurement wavelength range. Therefore the Cauchy model which is an empirical relationship between the refractive index and optical wavelength for transparent materials [85] was selected to describe the optical dispersion of the oxide barrier layer. The top layer in the three-layer model was the TNTA layer, which was first considered to be isotropic, so that it could be represented by the Cauchy model and parameters extracted for use as intelligent starting parameters in later fitting models incorporating anisotropy. The generated Ψ and Δ dispersions are shown in Figures 8(a) and 8(b). We can see from the dispersion that the generated delta dispersion matched the experimental data qualitatively, however, the generated Ψ data did not fit the experimental data very well. Uniaxial anisotropy was then added to the top Cauchy layer. Following the anisotropic fitting procedure provided by J. A.Woollam [86], the fit improved compared to the isotropic model. The generated Ψ and Δ dispersions for the anisotropic model are shown in Figures 8(c) and 8(d) where both the generated dispersions show a good match with the experimental data.

The uniaxial fit indicated a layer thickness of 440.9 nm for the TNTAs which is very close to the length of the nanotubes measured in the FESEM image (Figure 2(d)). Figure 9(a) shows the ordinary ($n_o$) and extraordinary ($n_e$) refractive indices of the anatase-phase TNTA layer determined from experimental data, as a function of wavelength. Both $n_o$ and $n_e$ for anatase-phase TNTAs show the same trend as bulk anatase [60, 61] but are smaller in magnitude due to the presence of air. The dispersion of the birefringence ($\Delta n$) was calculated and is displayed in Figure 9(c), which shows that the anatase-phase TNTAs are a positive birefringent material wherein the birefringence decreases with increasing wavelength. The same procedure was repeated rutile+anatase mixed phase TNTAs obtained by annealing at 750 °C, and the generated $\Psi$ and $\Delta$ dispersions are shown in Figures 8(e) and 8(f). The extracted refractive indices and birefringence dispersion rutile+anatase mixed phase TNTAs are shown in Figures 9(b) and 9(d), and found to be slightly higher than those of the pure anatase TNTAs. The magnitude of the birefringence of the anatase-phase TNTAs in this study (0.06 - 0.13) is higher than that of bulk anatase single crystals - which indicates the role of the nanotube geometry in achieving a higher optical anisotropy. On the other hand, the magnitude of the birefringence of the mixed-phase TNTAs in this study (0.06 - 0.15) is lower than that of bulk rutile single crystals due to the lack of phase-purity. The experimentally determined values for the refractive index and birefringence of the TNTAs in Figure 9 match better with the corresponding values calculated from BR effective medium approximations rather than the CYL EMA.

## 4. Conclusions

We obtained the refractive indices for the propagation of ordinary and extraordinary rays in titania nanotube arrays. We fabricated smooth TNTAs with specularly reflecting surfaces on a silicon wafer substrate and investigated their anisotropic optical properties using variable angle spectroscopic ellipsometry. The phonon confinement effect in laterally constricted grains constituting the nanotubes was analyzed by quantitative analysis of the Raman spectra, which revealed a distinct crystallite-size related broadening of Raman peaks of the TNTAs annealed at 500 °C. A uniaxial Cauchy model was used to extract optical constants from the experimental data. Comparison of FESEM imaging and ellipsometry analysis permitted us to deduce the thickness of the anatase NTAs layer to be 441 nm, and that of the mixed phase anatase+rutile TNTAs to be 570 nm. Both anatase-phase and mixed phase TNTAs exhibited positive

birefringence. In the visible-near infrared spectra range of 600 nm–1200 nm where $TiO_2$ has a negligible absorption, the ordinary refractive indices of anatase-phase TNTAs showed a decreasing trend from 1.87 to 1.73, and 2.00 to 1.87 for mixed phase TNTAs while the extraordinary refractive indices showed a similar trend decreasing from 2.00 to 1.85 for anatase-phase TNTAs and 2.15 to 1.97 for mixed phase anatase+rutile TNTAs.

## Acknowledgements

The authors thank NSERC, NRC-Canada, CFI and CMC Microsystems for direct and indirect (equipment) support. S.F. and B.D.W. thank Alberta Innovates Technology Futures for scholarship support.

## References

[1] Sousa C T, Leitao D C, Proenca M P, Ventura J, Pereira A M and Araujo J P 2014 Nanoporous alumina as templates for multifunctional applications *Appl. Phys. Rev.* **1** 031102

[2] Shankar K 2012 *Encyclopedia of Nanotechnology,* ed B Bhushan: pp 2742-55 (New York: Springer)

[3] Mohammadpour A and Shankar K 2010 Anodic $TiO_2$ nanotube arrays with optical wavelength-sized apertures *J. Mater. Chem.* **20** 8474-7

[4] Park J, Bauer S, von der Mark K and Schmuki P 2007 Nanosize and Vitality: $TiO_2$ Nanotube Diameter Directs Cell Fate *Nano Lett.* **7** 1686-91

[5] Chen X, Schriver M, Suen T and Mao S S 2007 Fabrication of 10 nm diameter $TiO_2$ nanotube arrays by titanium anodization *Thin Solid Films* **515** 8511-4

[6] Lim J H and Choi J 2007 Titanium Oxide Nanowires Originating from Anodically Grown Nanotubes: The Bamboo‐Splitting Model *Small* **3** 1504-7

[7] Mohammadpour A, Wiltshire B D, Zhang Y, Farsinezhad S, Askar A M, Kisslinger R, Ren Y, Kar P and Shankar K 2017 100-fold improvement in carrier drift mobilities in alkanephosphonate-passivated monocrystalline $TiO_2$ nanowire arrays *Nanotechnology* **28** 144001

[8] Farsinezhad S, Sharma H and Shankar K 2015 Interfacial band alignment for photocatalytic charge separation in $TiO_2$ nanotube arrays coated with CuPt nanoparticles *Phys. Chem. Chem. Phys.* **17** 29723-33

[9] Kar P, Farsinezhad S, Mahdi N, Zhang Y, Obuekwe U, Sharma H, Shen J, Semagina N and Shankar K 2016 Enhanced $CH_4$ yield by photocatalytic $CO_2$ reduction using $TiO_2$ nanotube arrays grafted with Au, Ru, and ZnPd nanoparticles *Nano Res.* **9** 3478-93

[10] Macak J M, Zlamal M, Krysa J and Schmuki P 2007 Self-Organized $TiO_2$ Nanotube Layers as Highly Efficient Photocatalysts *Small* **3** 300-4

[11] Rambabu Y, Manu J and Somnath C R 2015 Enhanced photoelectrochemical performance of multi-leg $TiO_2$ nanotubes through efficient light harvesting *J. Phys. D: Appl. Phys.* **48** 295302

[12] Dai G, Yu J and Liu G 2011 Synthesis and Enhanced Visible-Light Photoelectrocatalytic Activity of p−n Junction BiOI/$TiO_2$ Nanotube Arrays *J. Phys. Chem. C* **115** 7339-46

[13] Rand M J 1970 Spectrophotometric Thickness Measurement for Very Thin $SiO_2$ Films on Si *J. Appl. Phys.* **41** 787-90

[14] Mun K S, Alvarez S D, Choi W Y and Sailor M J 2010 A Stable, Label-free Optical Interferometric Biosensor Based on TiO2 Nanotube Arrays *ACS Nano* **4** 2070-6
[15] Roy P, Kim D, Lee K, Spiecker E and Schmuki P 2010 $TiO_2$ nanotubes and their application in dye-sensitized solar cells *Nanoscale* **2** 45-59
[16] Bella F, Lamberti A, Bianco S, Tresso E, Gerbaldi C and Pirri C F 2016 Floating, Flexible Polymeric Dye‐Sensitized Solar‐Cell Architecture: The Way of Near‐Future Photovoltaics *Advanced Materials Technologies* **1** 1600002
[17] Thakur U K, Askar A M, Kisslinger R, Wiltshire B D, Kar P and Shankar K 2017 Halide Perovskite Solar Cells Using Monocrystalline $TiO_2$ Nanorod Arrays as Electron Transport Layers: Impact of Nanorod Morphology *Nanotechnology* **DOI:10.1088/1361-6528/aa75ab**
[18] Bandara J, Shankar K, Basham J, Wietasch H, Paulose M, Varghese O K, Grimes C A and Thelakkat M 2011 Integration of TiO2 nanotube arrays into solid-state dye-sensitized solar cells *Eur. Phys. J-Appl. Phys.* **53** 20601
[19] Kongkanand A, Tvrdy K, Takechi K, Kuno M and Kamat P V 2008 Quantum Dot Solar Cells. Tuning Photoresponse through Size and Shape Control of CdSe−$TiO_2$ Architecture *J. Am. Chem. Soc.* **130** 4007-15
[20] Qin P, Paulose M, Dar M I, Moehl T, Arora N, Gao P, Varghese O K, Grätzel M and Nazeeruddin M K 2015 Stable and Efficient Perovskite Solar Cells Based on Titania Nanotube Arrays *Small* **11** 5533-9
[21] Kim H-S, Lee J-W, Yantara N, Boix P P, Kulkarni S A, Mhaisalkar S, Grätzel M and Park N-G 2013 High Efficiency Solid-State Sensitized Solar Cell-Based on Submicrometer Rutile $TiO_2$ Nanorod and CH3NH3PbI3 Perovskite Sensitizer *Nano Lett.* **13** 2412-7
[22] Bang-Ying Y, Ating T, Shu-Ping T, Ken-Tsung W, Yang Y, Chih-Wei C and Jing-Jong S 2008 Efficient inverted solar cells using $TiO_2$ nanotube arrays *Nanotechnology* **19** 255202
[23] Shankar K, Mor G K, Paulose M, Varghese O K and Grimes C A 2008 Effect of device geometry on the performance of $TiO_2$ nanotube array-organic semiconductor double heterojunction solar cells *J. Non-Cryst. Solids* **354** 2767-71
[24] Xiong H, Slater M D, Balasubramanian M, Johnson C S and Rajh T 2011 Amorphous $TiO_2$ nanotube anode for rechargeable sodium ion batteries *J. Phys. Chem. Lett.* **2** 2560-5
[25] Lu X, Wang G, Zhai T, Yu M, Gan J, Tong Y and Li Y 2012 Hydrogenated $TiO_2$ nanotube arrays for supercapacitors *Nano Lett.* **12** 1690-6
[26] Lamberti A and Pirri C F 2016 $TiO_2$ nanotube array as biocompatible electrode in view of implantable supercapacitors *J. Energ. Stor.* **8** 193-7
[27] Conti D, Lamberti A, Porro S, Rivolo P, Chiolerio A, Pirri C F and Ricciardi C 2016 Memristive behaviour in poly-acrylic acid coated $TiO_2$ nanotube arrays *Nanotechnology* **27** 485208
[28] Liu N, Lee K and Schmuki P 2013 Reliable Metal Deposition into $TiO_2$ Nanotubes for Leakage‐Free Interdigitated Electrode Structures and Use as a Memristive Electrode *Angew. Chem., Int. Ed.* **52** 12381-4
[29] Lin J, Liu K and Chen X F 2011 Synthesis of Periodically Structured Titania Nanotube Films and Their Potential for Photonic Applications *Small* **7** 1784-9
[30] Yip C T, Huang H T, Zhou L M, Xie K Y, Wang Y, Feng T H, Li J S and Tam W Y 2011 Direct and Seamless Coupling of $TiO_2$ Nanotube Photonic Crystal to Dye-Sensitized Solar Cell: A Single-Step Approach *Adv. Mater.* **23** 5624-8
[31] Guo M, Xie K Y, Lin J, Yong Z H, Yip C T, Zhou L M, Wang Y and Huang H T 2012 Design and coupling of multifunctional $TiO_2$ nanotube photonic crystal to nanocrystalline titania layer as semi-transparent photoanode for dye-sensitized solar cell *Energ. Environ. Sci.* **5** 9881-8

[32] Zhang X J, Han F, Shi B, Farsinezhad S, Dechaine G P and Shankar K 2012 Photocatalytic Conversion of Diluted $CO_2$ into Light Hydrocarbons Using Periodically Modulated Multiwalled Nanotube Arrays *Angew. Chem.-Int. Edit.* **51** 12732-5
[33] Zhang Z H, Zhang L B, Hedhili M N, Zhang H N and Wang P 2013 Plasmonic Gold Nanocrystals Coupled with Photonic Crystal Seamlessly on $TiO_2$ Nanotube Photoelectrodes for Efficient Visible Light Photoelectrochemical Water Splitting *Nano Lett.* **13** 14-20
[34] Zhang Z H, Yang X L, Hedhili M N, Ahmed E, Shi L and Wang P 2014 Microwave-Assisted Self-Doping of $TiO_2$ Photonic Crystals for Efficient Photoelectrochemical Water Splitting *ACS Appl. Mater. Interfaces* **6** 691-6
[35] Kondo T, Hirano S, Yanagishita T, Nguyen N T, Schmuki P and Masuda H 2016 Two-dimensional photonic crystals based on anodic porous $TiO_2$ with ideally ordered hole arrangement *Appl. Phys. Express* **9** 102001
[36] Wang G, Wang J, An Y Y and Wang C W 2016 Anodization fabrication of 3D $TiO_2$ photonic crystals and their application for chemical sensors *Superlattices Microstruct.* **100** 290-5
[37] Dickson W, Wurtz G A, Evans P, O'Connor D, Atkinson R, Pollard R and Zayats A V 2007 Dielectric-loaded plasmonic nanoantenna arrays: A metamaterial with tuneable optical properties *Phys. Rev. B* **76** 115411
[38] Lu W T and Sridhar S 2008 Superlens imaging theory for anisotropic nanostructured metamaterials with broadband all-angle negative refraction *Phys. Rev. B* **77** 233101
[39] Starko-Bowes R, Atkinson J, Newman W, Hu H, Kallos T, Palikaras G, Fedosejevs R, Pramanik S and Jacob Z 2015 Optical characterization of epsilon-near-zero, epsilon-near-pole, and hyperbolic response in nanowire metamaterials *Journal of the Optical Society of America B-Optical Physics* **32** 2074-80
[40] Yuen K P, Law M F, Yu K W and Sheng P 1998 Enhancement of optical nonlinearity through anisotropic microstructures *Opt. Commun.* **148** 197-207
[41] Tiginyanu I M, Kravetsky I V, Monecke J, Cordts W, Marowsky G and Hartnagel H L 2000 Semiconductor sieves as nonlinear optical materials *Appl. Phys. Lett.* **77** 2415-7
[42] Menon L, Lu W T, Friedman A L, Bennett S P, Heiman D and Sridhar S 2008 Negative index metamaterials based on metal-dielectric nanocomposites for imaging applications *Appl. Phys. Lett.* **93** 123117
[43] Kabashin A V, Evans P, Pastkovsky S, Hendren W, Wurtz G A, Atkinson R, Pollard R, Podolskiy V A and Zayats A V 2009 Plasmonic nanorod metamaterials for biosensing *Nat. Mater.* **8** 867-71
[44] Jahani S and Jacob Z 2016 All-dielectric metamaterials *Nat. Nanotechnol.* **11** 23-36
[45] Moitra P, Yang Y, Anderson Z, Kravchenko I I, Briggs D P and Valentine J 2013 Realization of an all-dielectric zero-index optical metamaterial *Nat Photon* **7** 791-5
[46] Vynck K, Felbacq D, Centeno E, Căbuz A I, Cassagne D and Guizal B 2009 All-Dielectric Rod-Type Metamaterials at Optical Frequencies *Phys. Rev. Lett.* **102** 133901
[47] Kallos E, Chremmos I and Yannopapas V 2012 Resonance properties of optical all-dielectric metamaterials using two-dimensional multipole expansion *Phys. Rev. B* **86** 245108
[48] Ahmadi A and Mosallaei H 2008 Physical configuration and performance modeling of all-dielectric metamaterials *Phys. Rev. B* **77** 045104
[49] Krasnok A, Makarov S, Petrov M, Savelev R, Belov P and Kivshar Y 2015 Towards all-dielectric metamaterials and nanophotonics(vol 9502) p 950203-17
[50] Zhao Q, Zhou J, Zhang F and Lippens D 2009 Mie resonance-based dielectric metamaterials *Mater. Today* **12** 60-9
[51] Tokman M D and Erukhimova M A 2015 Anisotropy-Induced Transparency in Optically Dense Media *Radiophys. Quantum Electron.* **57** 821-36

[52] Corbitt S J, Francoeur M and Raeymaekers B 2015 Implementation of optical dielectric metamaterials: A review *J. Quant. Spectrosc. Ra.* **158** 3-16
[53] Polo J A and Lakhtakia A 2008 *Nanostructured Thin Films,* ed G B Smith and A Lakhtakia
[54] Faryad M and Lakhtakia A 2013 Prism-coupled excitation of Dyakonov-Tamm waves *Opt. Commun.* **294** 192-7
[55] Zapata-Rodriguez C J, Miret J J, Sorni J A and Vukovic S 2013 Propagation of Dyakonon Wave-Packets at the Boundary of Metallodielectric Lattices *IEEE J. Sel. Top. Quantum Electron.* **19** 4601408
[56] Takayama O, Artigas D and Torner L 2014 Lossless directional guiding of light in dielectric nanosheets using Dyakonov surface waves *Nat. Nanotechnol.* **9** 419-24
[57] Miret J J, Sorni J A, Naserpour M, Ardakani A G and Zapata-Rodriguez C J 2016 Nonlocal dispersion anomalies of Dyakonov-like surface waves at hyperbolic media interfaces *Photonic. Nanostruct.* **18** 16-22
[58] John K A, Naduvath J, Mallick S, Shripathi T, Thankamoniamma M and Philip R R 2015 A novel cost effective fabrication technique for highly preferential oriented $TiO_2$ nanotubes *Nanoscale* **7** 20386-90
[59] Lee S, Park I J, Kim D H, Seong W M, Kim D W, Han G S, Kim J Y, Jung H S and Hong K S 2012 Crystallographically preferred oriented $TiO_2$ nanotube arrays for efficient photovoltaic energy conversion *Energ. Environ. Sci.* **5** 7989-95
[60] Jellison G E, Modine F A and Boatner L A 1997 Measurement of the optical functions of uniaxial materials by two-modulator generalized ellipsometry: rutile ($TiO_2$) *Opt. Lett.* **22** 1808-10
[61] Jellison G E, Boatner L A, Budai J D, Jeong B S and Norton D P 2003 Spectroscopic ellipsometry of thin film and bulk anatase ($TiO_2$) *J. Appl. Phys.* **93** 9537-41
[62] Farsinezhad S, Mohammadpour A, Dalrymple A N, Geisinger J, Kar P, Brett M J and Shankar K 2013 Transparent Anodic $TiO_2$ Nanotube Arrays on Plastic Substrates for Disposable Biosensors and Flexible Electronics *J. Nanosci. Nanotechnol.* **13** 2885-91
[63] Farsinezhad S, Dalrymple A N and Shankar K 2014 Toward single-step anodic fabrication of monodisperse $TiO_2$ nanotube arrays on non-native substrates *Phys. Status Solidi A* **211** 1113-21
[64] Crawford G A and Chawla N 2009 Tailoring $TiO_2$ nanotube growth during anodic oxidation by crystallographic orientation of Ti *Scr. Mater.* **60** 874-7
[65] Leonardi S, Li Bassi A, Russo V, Di Fonzo F, Paschos O, Murray T M, Efstathiadis H and Kunze J 2011 $TiO_2$ nanotubes: interdependence of substrate grain orientation and growth characteristics *J. Phys. Chem. C* **116** 384-92
[66] Harrick N J 1971 Determination of Refractive Index and Film Thickness from Interference Fringes *Appl. Opt.* **10** 2344-9
[67] Varghese O K, Gong D, Paulose M, Grimes C A and Dickey E C 2003 Crystallization and high-temperature structural stability of titanium oxide nanotube arrays *J. Mater. Res.* **18** 156-65
[68] Kar P, Zhang Y, Farsinezhad S, Mohammadpour A, Wiltshire B D, Sharma H and Shankar K 2015 Rutile phase n- and p-type anodic titania nanotube arrays with square-shaped pore morphologies *Chem. Commun.* **51** 7816-9
[69] Li W, Ni C, Lin H, Huang C and Shah S I 2004 Size dependence of thermal stability of $TiO_2$ nanoparticles *J. Appl. Phys.* **96** 6663-8
[70] Ohsaka T, Izumi F and Fujiki Y 1978 Raman spectrum of anatase, $TiO_2$ *J. Raman Spectrosc.* **7** 321-4
[71] Attar A S and Hassani Z 2015 Fabrication and Growth Mechanism of Single-crystalline Rutile $TiO_2$ Nanowires by Liquid-phase Deposition Process in a Porous Alumina Template *J. Mater. Sci. Technol.* **31** 828-33

[72] Grimes C A and Mor G K 2009 *$TiO_2$ nanotube arrays: synthesis, properties, and applications* (New York: Springer)
[73] Sahoo S, Arora A and Sridharan V 2009 Raman line shapes of optical phonons of different symmetries in anatase $TiO_2$ nanocrystals *J. Phys. Chem. C* **113** 16927-33
[74] Lottici P, Bersani D, Braghini M and Montenero A 1993 Raman scattering characterization of gel-derived titania glass *J. Mater. Sci.* **28** 177-83
[75] Di Bartolo B 2010 *Optical interactions in solids* (Singapore: World Scientific Publishing Co.)
[76] Wang H, Liu X L, Wang L P and Zhang Z M 2013 Anisotropic optical properties of silicon nanowire arrays based on the effective medium approximation *Int. J. Therm. Sci.* **65** 62-9
[77] Shankar K, Mor G K, Prakasam H E, Yoriya S, Paulose M, Varghese O K and Grimes C A 2007 Highly-ordered $TiO_2$ nanotube arrays up to 220 µm in length: use in water photoelectrolysis and dye-sensitized solar cells *Nanotechnology* **18** 065707
[78] Farsinezhad S, Waghmare P R, Wiltshire B D, Sharma H, Amiri S, Mitra S K and Shankar K 2014 Amphiphobic surfaces from functionalized $TiO_2$ nanotube arrays *RSC Adv.* **4** 33587-98
[79] Ninham B W and Sammut R A 1976 Refractive index of arrays of spheres and cylinders *J. Theor. Biol.* **56** 125-49
[80] Ngoc Tai L, Van Chien N, Thi Hoa D, Le Hong Hoang T, Duy Long P, Hung Manh D, Dinh Lam V and Van Hong L 2014 Optical properties of $TiO_2$ nanotube arrays fabricated by the electrochemical anodization method *Adv. Nat. Sci.: Nanosci. Nanotechnol.* **5** 015004
[81] Tanemura S, Miao L, Jin P, Kaneko K, Terai A and Nabatova-Gabain N 2003 Optical properties of polycrystalline and epitaxial anatase and rutile $TiO_2$ thin films by rf magnetron sputtering *Appl. Surf. Sci.* **212–213** 654-60
[82] Woollam J A, Snyder P G and Rost M C 1988 Variable angle spectroscopic ellipsometry: a non-destructive characterization technique for ultrathin and multilayer materials *Thin Solid Films* **166** 317-23
[83] Azzam R M A and Bashara N M 1977 Ellipsometry and Polarized Light (Amsterdam:North-Holland)
[84] Flueraru C, Schrader S, Motschmann H and Zauls V 2000 Sensitivity analysis of ellipsometry applied to uniaxial optical films *Thin Solid Films* **379** 15-22
[85] Jorgensen B 1997 *The theory of dispersion models* (London:Chapman & Hall)
[86] Woollam J A 2002 *Guide to using WVASE32* (Lincoln: JA Woollam)

## LIST OF FIGURES AND FIGURE CAPTIONS

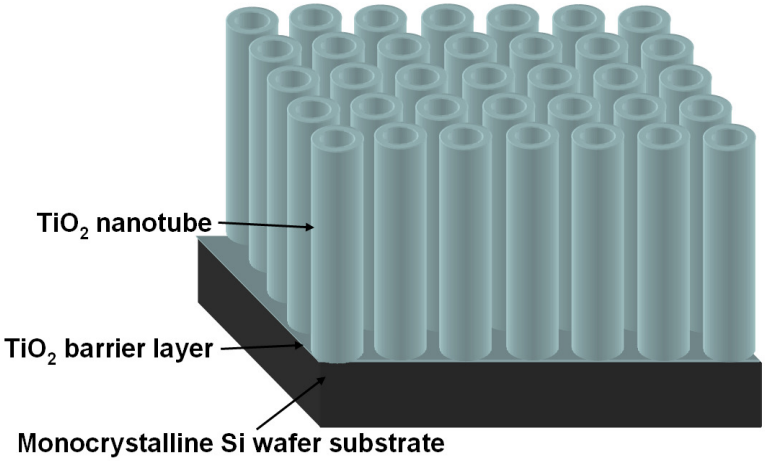


**Figure 1.** Schematic illustration of anodically formed $TiO_2$ nanotube arrays on a Si wafer substrate.

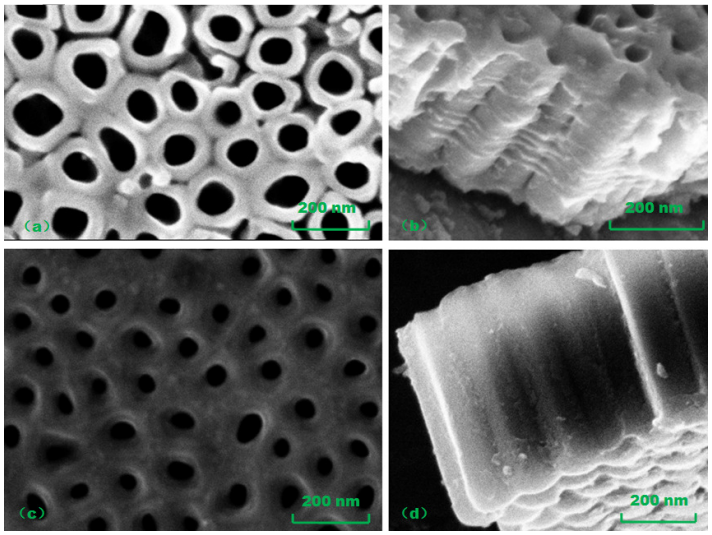


**Figure 2.** FESEM images of TNTAs anodized at 40 V for 20 min **(a)** Top view and **(b)** Cross-section for samples annealed at 500 °C for 2.5 hours; **(c)** Top-view and **(d)** Cross-section for samples annealed at 750 °C for 2.5 hours.

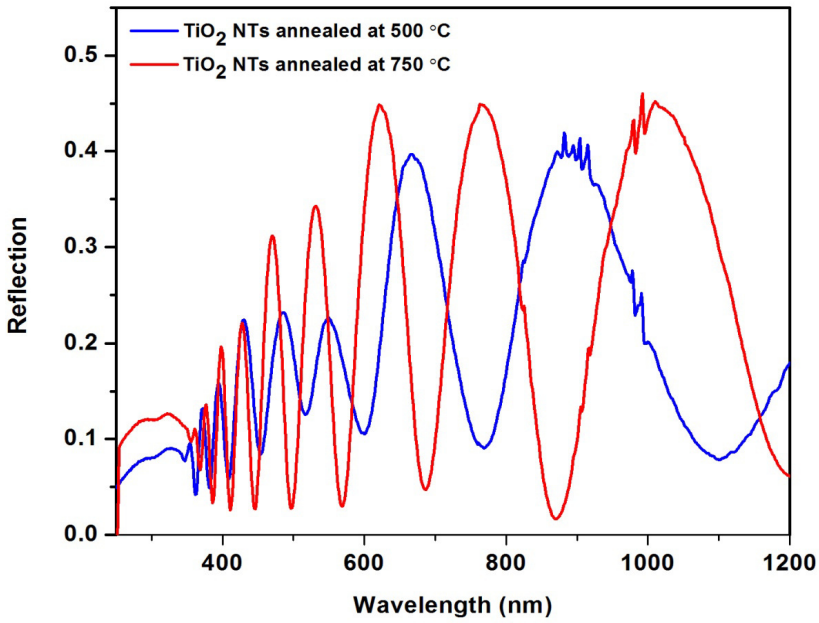


**Figure 3.** Specular reflection spectra of TNTAs measured in response to unpolarized light incident on the TNTAs at a 20° angle of incidence. The high reflectance values and clear interferometric fringes demonstrate the high optical quality of the TNTA samples.

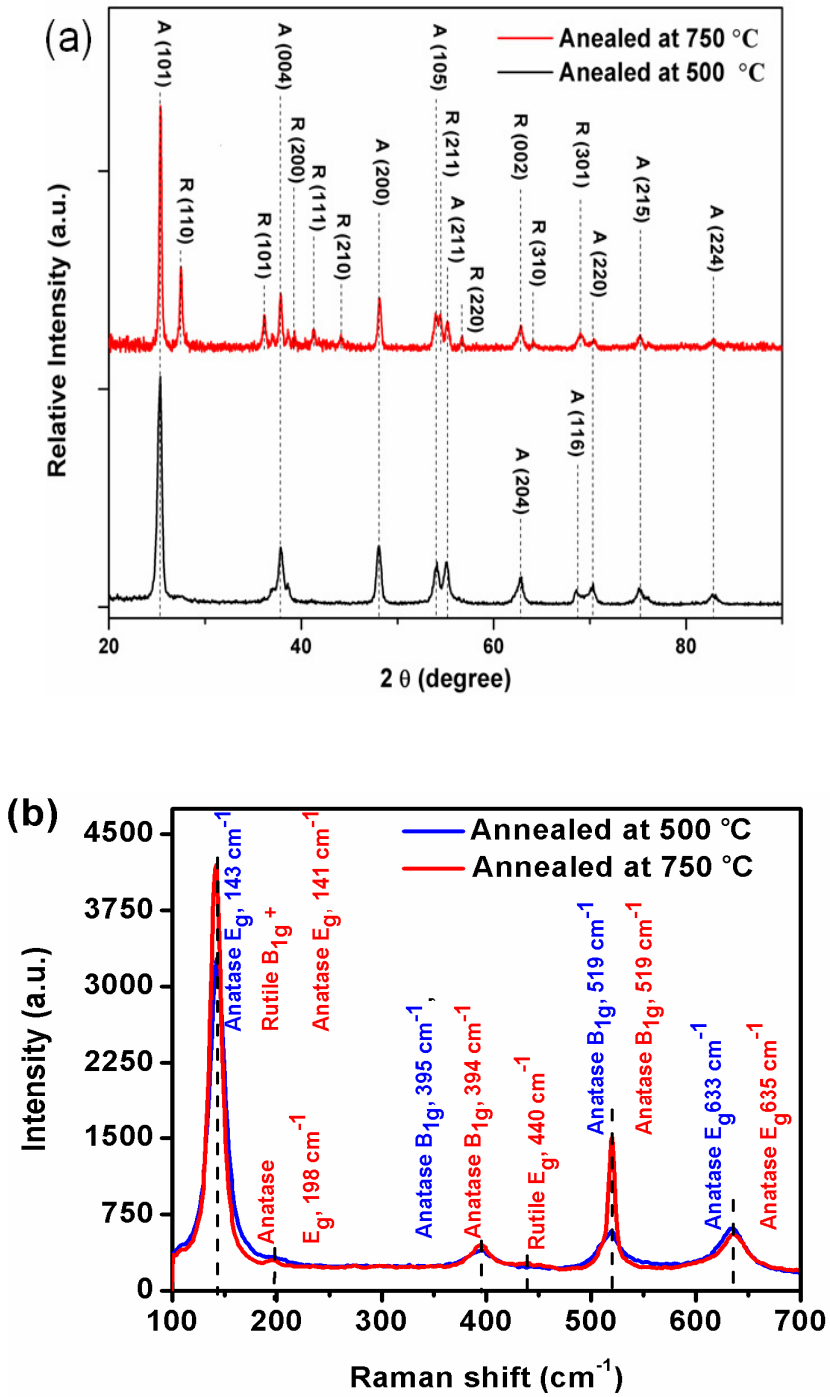


**Figure 4. (a)** XRD patterns and **(b)** Raman spectra of TNTAs anodized at 40 V for 20 min and furnace annealed at 500 °C and 750 °C for 2.5 hours.

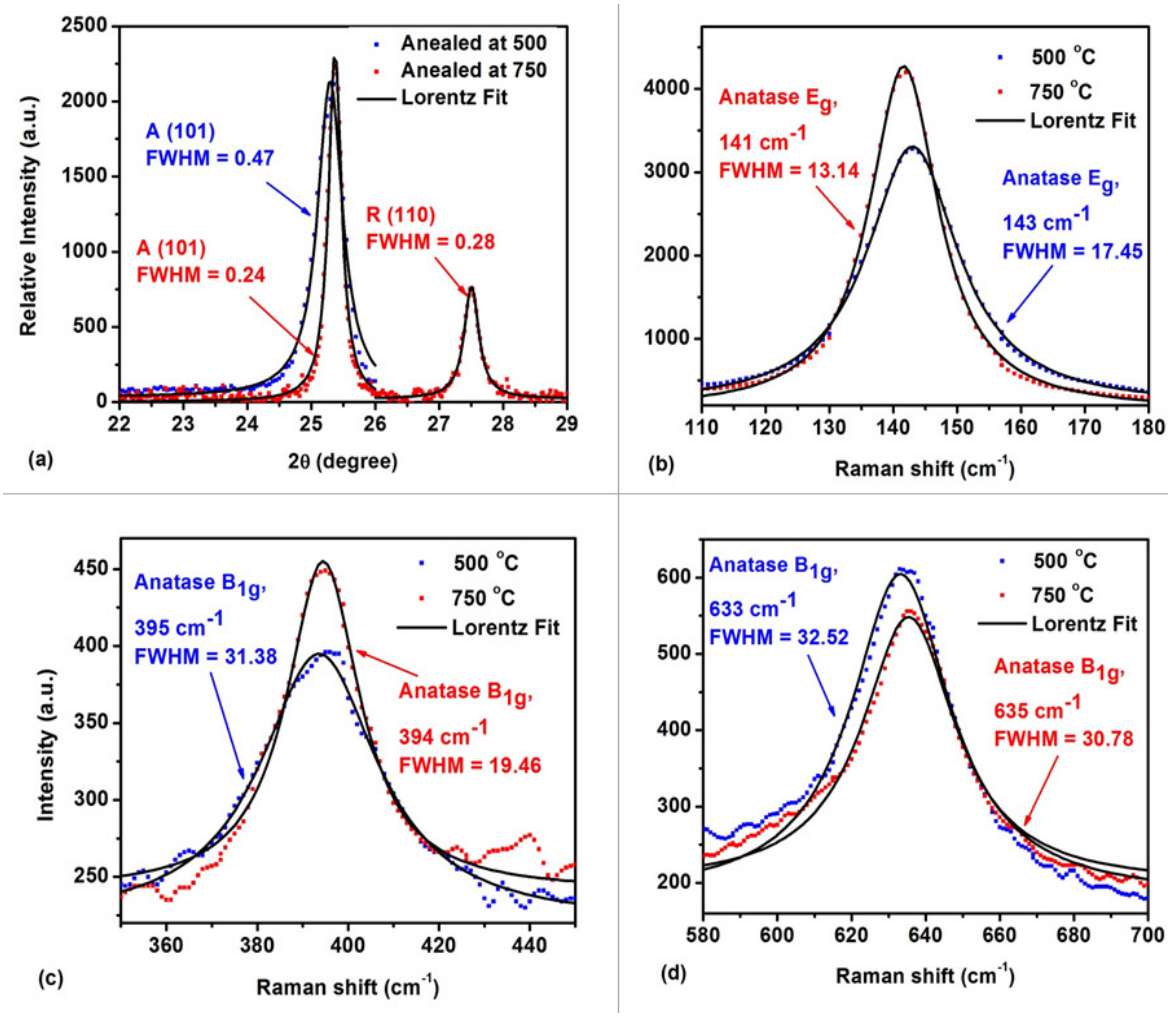


**Figure 5. (a)** XRD patterns and **(b)**, **(c)** and **(d)** are Lorentzian fits of the two $E_g$ and $B_{1g}$ Raman modes of TNTAs annealed at 500 °C and 750 °C.

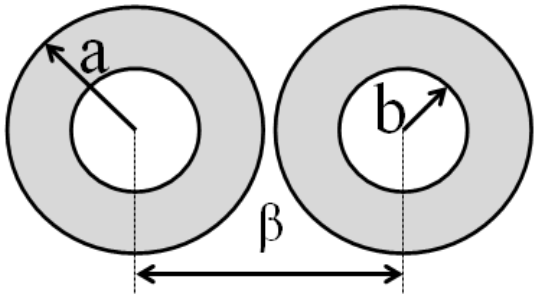


**Figure 6.** Geometry of the nanotube architecture used in effective medium calculations.

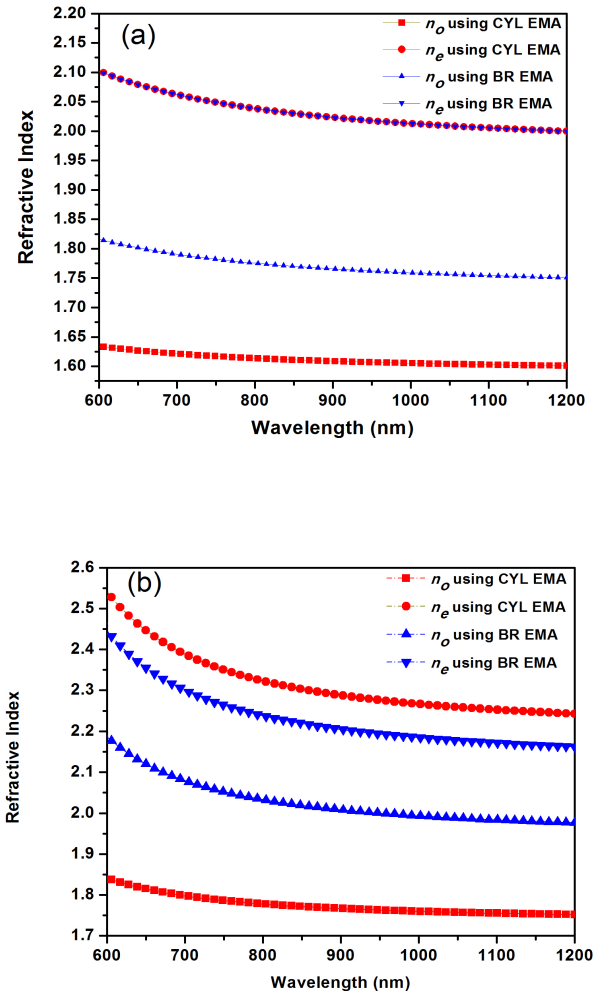


**Figure 7.** Anisotropic permittivity of TNTAs constituted by **(a)** Anatase-phase $TiO_2$ and **(b)** Rutile-phase $TiO_2$, calculated using the BR and CYL effective medium approximations, see Eqns (1) through (6).

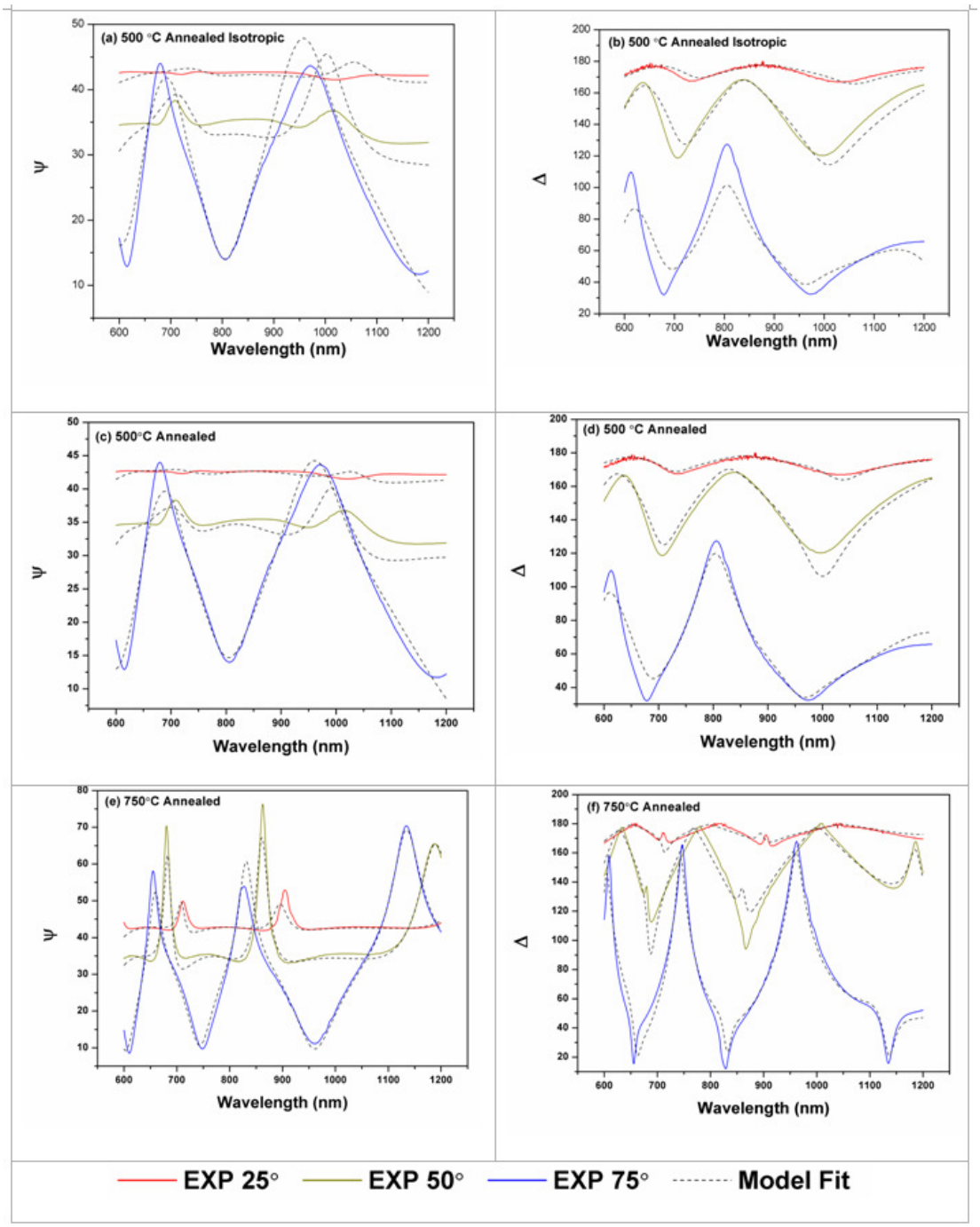


**Figure 8.** Ellipsometric dispersion patterns including measured experimental data (solid lines) and generated curves from best-fit models (dotted lines) for three different angles of incidence. Panels **(a)**, **(c)** and **(e)** correspond to anatase-phase TNTAs while panels **(b)**, **(d)** and **(f)** correspond to rutile+anatase mixed phase TNTAs. While panels **(a)** and **(b)** show the results of isotropic fits to the Ψ and Δ spectra of anatase-phase TNTAs, panels **(c)** and **(d)** show the anisotropic fitting data for anatase-phase TNTAs. **(e)** and **(f)** show the experimental data and anisotropic curve fits for rutile+anatase mixed phase TNTAs.

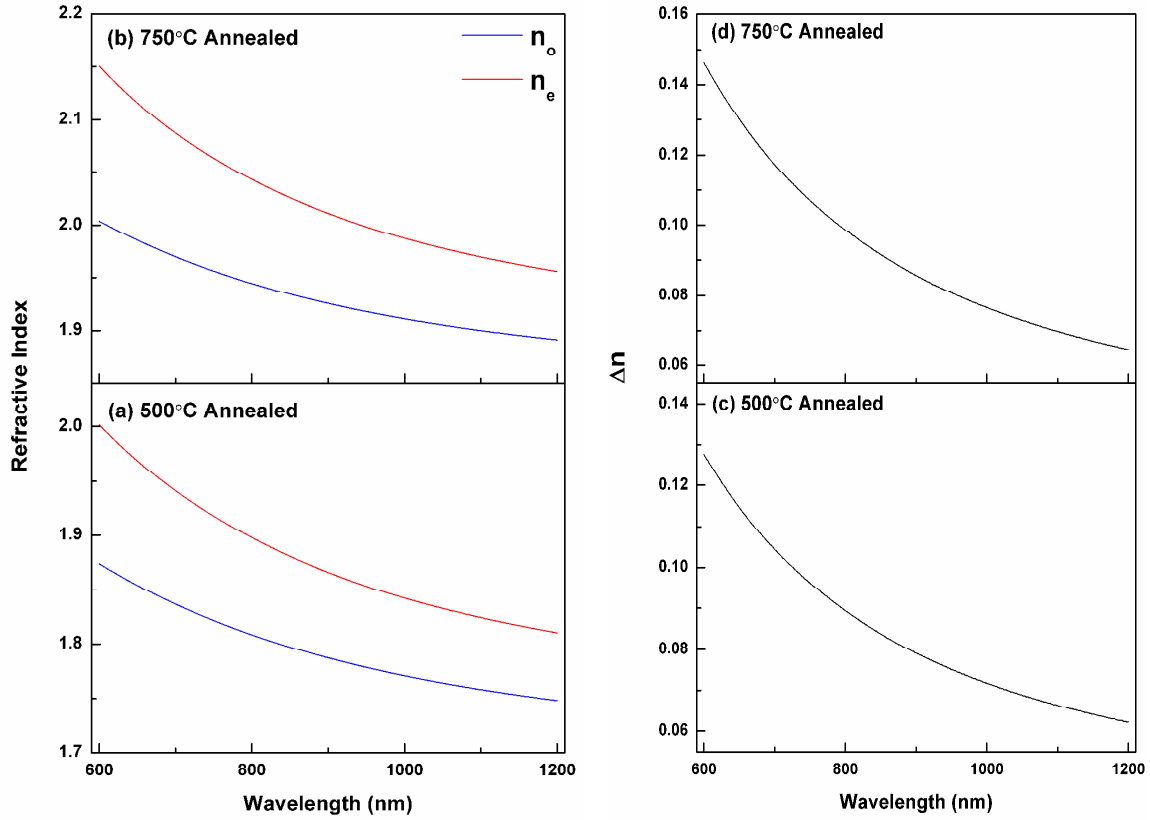


**Figure 9.** Ordinary and extraordinary refractive indices dispersion pattern of **(a)** anatase TNTAs and **(b)** rutile+anatase mixed-phase TNTAs. And birefringence dispersion patterns for **(c)** anatase TNTAs and **(d)** rutile+anatase mixed-phase TNTAs.